Received: 8 September 2020 | Revised: 30 November 2020 | Accepted: 11 January 2021

IET Science, Measurement & Technology

DOI: 10.1049/smt2.12022

The Institution of Engineering and Technology WILEY

ORIGINAL RESEARCH PAPER

Solving 1D non-linear magneto quasi-static Maxwell's equations using neural networks

Marco Baldan[1] | **Giacomo Baldan**[2] | **Bernard Nacke**[1]

[1] Institute of Electrotechnology, Leibniz Universität Hannover, Hanover, Germany

[2] Department of Aerospace Engineering, Politecnico di Milano, Milan, Italy

Correspondence
Marco Baldan, Institute of Electrotechnology, Leibniz Universität Hannover, Hanover, Germany.
Email: baldan@etp.uni-hannover.de

Funding information
Gottfried Wilhelm Leibniz Universität Hannover

Abstract

Electromagnetics (EM) can be described, together with the constitutive laws, by four PDEs, called Maxwell's equations. "Quasi-static" approximations emerge from neglecting particular couplings of electric and magnetic field related quantities. In case of slowly time varying fields, if inductive and resistive effects have to be considered, whereas capacitive effects can be neglected, the magneto quasi-static (MQS) approximation applies. The solution of the MQS Maxwell's equations, traditionally obtained with finite differences and elements methods, is crucial in modelling EM devices. In this paper, the applicability of an unsupervised deep learning model is studied in order to solve MQS Maxwell's equations, in both frequency and time domain. In this framework, a straightforward way to model hysteretic and anhysteretic non-linearity is shown. The introduced technique is used for the field analysis in the place of the classical finite elements in two applications: on the one hand, the *B*–*H* curve inverse determination of AISI 4140, on the other, the simulation of an induction heating process. Finally, since many of the commercial FEM packages do not allow modelling hysteresis, it is shown how the present approach could be further adopted for the inverse magnetic properties identification of new magnetic flux concentrators for induction applications.

1 | INTRODUCTION

The solution of partial differential equations (PDEs) plays an essential role in engineering and scientific applications. Traditional methods, such as finite elements (FEs), finite volumes (FVs), and finite differences (FDs), rely on discretizing the domain into a set of mesh points in which the solution is calculated [1]. Interest of solving PDEs using neural network (NN)-based methods has a relatively long history that started in the 90s [2, 3]. Lagaris et al. [3] used trial functions, based on a single layer perceptron, to approximate the solutions of ODEs and PDEs. So doing the NN is treated as a continuous function, whose inputs are the variables the solution depends on. This approach greatly benefits from the differentiability of NNs via backpropagation [4]. Training is performed in order to minimize the solution residuals inside the domain and on the boundaries.

Recently, deep learning emerges as a powerful technique in many applications, including computer vision, speech recognition, natural language process, and bioinformatics. There is an increasing new interest in the literature for the application of deep learning methods for scientific computation, including solving partial differential equations [5–7]. This is mainly due to substantial improvements in the hardware used to run NNs, and to the discovery of better practices of training [8]. In last years, with an analogous approach to that already presented in [3], training multilayer perceptron-style NNs have been successful in tackling a much greater variety of PDEs, also with complex domains and BCs. For instance, Berg et al. [6] showed that, in contrast to most numerical PDE techniques, NNs are suitable for high-dimensional problems and complicated domains. In [9], Raissi et al. introduced 'physics informed neural networks (PINNs)" successfully solving Schrödinger's and Burgers' equations. Furthermore, PINNs were extended to fractional PINNs (fPINNs) to solve fractional advection-diffusion equations [11] and, based on this paradigm, Lu et al. [10] developed the DeepXDE library, capable of solving a wide range of differential equations. Dwivedi et al. in [12, 13] proposed 'physics informed extreme learning machine (PIELM)", a rapid version of PINNs that can be applied to stationary and time dependent linear

partial differential equations. They also discussed the limitations of PIELM, namely the difficulty in solving differential equations where the solution has sharp gradients or discontinuity. The suggested DPIELM (Distributed PIELM) takes inspiration from the finite volumes method in which the whole computational domain is partitioned into multiple cells and governing equations are solved at each cell. Despite very good results have been achieved by DPIELM [12], in contrast to PINNs, this method requires a discretization of the domain. Furthermore, Meng et al. [14] proposed MPINNs (Multi-fidelity PINNs) in order to solve PDEs in case where a combination of abundant but less accurate "low-fidelity", and sparse but more accurate "high-fidelity" data are available. In alternative to the presented approaches, recently, also convolutional neural networks (CNNs) have begun to gain interest. Using common techniques in computer vision, treating the known terms and solutions of PDEs on rectangular meshes as though they were images approaches the task of solving a PDE. In this case, CNNs end up solving large linear systems. Tompson et al. [15] employed a CNN in order to accelerate Eulerian fluid simulations, and presented a data-driven approach for approximate inference of the linear system used to ensure the Navier–Stokes incompressibility condition. Also Xiao et al. [16] introduced a CNN with the capability of solving a Poisson equation in order to predict the pressure, given the discretization structure and the intermediate velocities as input. The applicability of CNNs for the solution of the Poisson equation has been recently widened in ref. [8] to arbitrary Dirichlet boundary conditions and grid parameters.

The use of NNs and CNNs for solving PDEs in engineering applications has been mainly focused to fluid dynamics [9, 15–18]. However, few works dealing with electromagnetism do exist [19–22]. However, almost all of them are limited to electrostatics. Rumuhalli et al. [19] proposed a finite element neural network (FENN) that embeds finite element models into a neural network format. FENN was successfully used to solve inverse problem based on Poisson's equation. Also the works presented in [20, 22] concern electrostatic problems, here by making use of CNNs. Tang et al. [20] highlighted the flexibility of CNNs in case of complex distributions of excitation sources and dielectric constants. Zhang et al. [22] could decrease, in comparison to FD method, the calculation time of factor 10 in determining the I–V curve for a PN junction. Finally, Bartlett [21] solved Maxwell's equations in frequency domain in case of a non-magnetic, linear material. The structure of his model is similar to a generative adversarial network: the first part of the model reminds a "generator" since it maps the space-distribution of permittivity to the electric field distribution. The second part, i.e. the "discriminator", evaluates how physically realistic the generators' outputs are. Despite this approach outperforms, in terms of calculation time, of factor 10 a finite difference solution, it neglects the imaginary part of all phasors. Moreover, the implementation of the magnetic non-linearity has not been investigated. The solution in time domain has been to not analysed too. To authors' best knowledge, the solution of Maxwell's equations using deep learning, in non-static conditions, has actually not been studied so far. This work attempts to bridge this gap.

Magnetic flux concentrators (MFCs) are materials, other than copper coil, that are used in induction systems to alter the flow of the magnetic field. The benefits of using magnetic flux concentrators include improvement of induction coil and process efficiency, increase of power factor, reduction of coil current, precise control of the magnetic field and resulting heat pattern [23, 24]. There are three families of MFCs: ferrites, steel laminations, and soft magnetic composites (SMCs). Soft magnetic composites are the most widely used, since they can work in a large range of frequencies with acceptable losses. However, temperatures higher than 200 °C can lead to irreparable damages, which worsen the material performances. Therefore, in designing an induction heating system equipped with SMCs, it is fundamental to know their properties to correctly estimate their working temperature. SMCs are made from ferrous particles covered with a thin insulation layer, mixed with organic or inorganic binder, and pressed at high pressure. Recently, the possibility of using generative manufacturing for the production of MFCs has been investigated [25]. There is a growing interest in the production of new MFCs, using different mixtures and combinations of ferrous particles with binder materials, and with it the necessity of their properties identification. Generally, SMCs have a high electrical resistivity and a middle magnetic permeability. Therefore, hysteretic losses play a non-negligible role, which must be modelled by an inverse properties identification or, more in general, whenever the temperature distribution within the SMC is needed.

The paper is organized as followed. In Section 2, making use of NNs, Maxwell's equations are solved in frequency domain firstly considering linear materials, and then taking ferromagnetic behaviours into account (non-linear B–H relationship and hysteresis losses). Section 3 is dedicated to the solution of Maxwell's equations in time domain instead. A straightforward approach for modelling hysteresis is described. Finally, in Section 4, employing the models presented in Sections 2 and 3, we will show that the proposed approach can replace the FDs and FEs simulations in two exemplary cases. In the first case the B–H curve of AISI 4140 is determined inverting the induced voltage at the secondary coil. Second, still using only neural networks, coupling the solution of the Maxwell's and Fourier's equations allows to find the distribution of temperature within a steel work-piece. Results of simulations have been validated on the base of real experiments. In the end, it is discussed how the approach could be used for the inverse magnetic properties identification of new flux guiding materials for induction heating.

2 | SOLVING MAXWELL'S EQUATIONS IN FREQUENCY DOMAIN

2.1 | Linear Maxwell's equations

Maxwell's four equations are as follow [26]:

$$\nabla \times \mathbf{H} = \mathbf{J} + \frac{\partial \mathbf{D}}{\partial t} \tag{1}$$

$$\nabla \cdot \mathbf{B} = 0 \tag{2}$$

$$\nabla \times \mathbf{E} = -\frac{\partial \mathbf{B}}{\partial t} \tag{3}$$

$$\nabla \cdot \mathbf{D} = \rho \tag{4}$$

In addition there are the constitutive laws: $\mathbf{J} = \sigma\mathbf{E}$, $\mathbf{B} = \mu\mathbf{H} = \mu_0(\mathbf{H} + \mathbf{M})$, and $\mathbf{D} = \epsilon\mathbf{E}$. The electromagnetic quantities involved in the equations are the electric field intensity $\mathbf{E}$, the electric flux density $\mathbf{D}$, the magnetic field intensity $\mathbf{H}$, the magnetic flux density $\mathbf{B}$, the magnetization field $\mathbf{M}$, the surface current density $\mathbf{J}$, the volume charge density ρ. We also define the magnetic permeability μ, the dielectric permittivity ϵ, and the electric conductivity σ. Since we will deal with ferromagnetic materials (mostly metals), frequencies not higher than a hundred of kHz, and small size setups ($\sim 10^{-1}$ m), the last term of Equation (1) could be neglected (magneto quasi-static—MQS—approximation of the Maxwell's equations) [27–30]. This formulation, just to name a few examples, is broadly used in the field analysis of induction heating [31, 32], inverse *B–H* identification [33], power transmission lines [34], electrical machines [35]. Combining Equation (3) with the first constitutive law and Equation (1) leads to:

$$\nabla \times \frac{1}{\sigma}\nabla \times \mathbf{H} = -\frac{\partial \mathbf{B}}{\partial t} \tag{5}$$

If the material is uniform, isotropic, and linear, thanks to Equation (2) and the second constitutive law, Equation (5) becomes:

$$\frac{1}{\mu\sigma}\nabla^2\mathbf{B} = \frac{\partial \mathbf{B}}{\partial t} \tag{6}$$

In a steady-state frequency domain solution, $B(t)$ is a phasor $\underline{B} = B_{\mathrm{Re}} + jB_{\mathrm{Im}} = |\underline{B}| \exp^{j\phi_B}$, where $B(t) = \Re(|\underline{B}|\ e^{j\omega t + \phi_B})$, and $\omega = 2\pi f$, with f the frequency. Equation (6) transforms into:

$$\frac{1}{\mu\sigma}\nabla^2\underline{B} = j\omega\underline{B} \tag{7}$$

The solution of Equation (7) occurs employing NNs, similarly to what done in [3, 9]. That is, the neural network itself or a priori defined trial function, which in turn depends on the neural network, describe the PDE's solution within the domain. In this framework, backpropagation [4] makes the differentiation of the NN's outputs with respect to inputs straightforward. The number of inputs in the NN equals the number of variables of the PDE. In this particular case the NN has two outputs ($\mathcal{N}_1(x)$, $\mathcal{N}_2(x)$), describing the real and the imaginary part of the magnetic flux density, respectively. In order to automatically satisfy the Dirichlet boundary conditions, trial functions (T_{f}) are adopted. This means that trial functions, which depend on the NN, will provide the PDE's solution. Nothing prevents different outputs to use different trial functions. Indeed, trial functions take Dirichlet boundary conditions into account that, in the case of the real and imaginary part of $\underline{B}$, can be different. We will analyse a 1D case (i.e. there is a single space coordinate, x, physical variables are scalars) with a solution domain (0; 1) m. The first case is an explanatory instance, in which the Dirichlet boundary conditions are assumed to be:

$$\mathrm{BCs} = \begin{cases} \Re(\underline{B}(0)) = 1,\ \Re(\underline{B}(1)) = 0 \\ \Im(\underline{B}(0)) = 0,\ \Im(\underline{B}(1)) = 0 \end{cases} \tag{8}$$

In order to automatically satisfy Equation (8), the trial functions for the real ($T_{\mathrm{f,\,Re}}$) and imaginary ($T_{\mathrm{f,\,Im}}$) parts value:

$$\begin{aligned} T_{\mathrm{f,\,Re}}(x) &= \mathcal{N}_1(x)\ m_{\mathrm{Re}}\ x\ (1-x) + (1-x) \\ T_{\mathrm{f,\,Im}}(x) &= \mathcal{N}_2(x)\ m_{\mathrm{Im}}\ x\ (1-x) \end{aligned} \tag{9}$$

In fact, regardless of the outputs of the neural network $\mathcal{N}_{1,2}(x)$, $T_{\mathrm{f,\,Re}}(0) = 1$ and $T_{\mathrm{f,\,Re}}(1) = 0$, while $T_{\mathrm{f,\,Im}}(0) = 0$ and $T_{\mathrm{f,\,Im}}(1) = 0$, as defined in Equation (8). Here m_{Re} and m_{Im} are constants set to 10. They are user-defined parameters that allow a better functioning of the neural network, since its outputs ($\mathcal{N}_1(x)$, $\mathcal{N}_2(x)$, ...) are typically not higher than 1. Training points are uniformly distributed inside the domain where the PDE needs to be solved. The loss function is the residual of the real and imaginary part calculated over all training points (TP):

$$\begin{aligned} \mathcal{L}_{\mathrm{PDE}} = \frac{1}{\mathrm{TP}}\sum_{\mathrm{TP}} \Bigg(&\left\| \frac{1}{\mu\sigma}\nabla^2 T_{\mathrm{f,Re}} + \omega T_{\mathrm{f,Im}} \right\|_2 + \\ &\left\| \frac{1}{\mu\sigma}\nabla^2 T_{\mathrm{f,Im}} - \omega T_{\mathrm{f,Re}} \right\|_2 \Bigg) \end{aligned} \tag{10}$$

For example, having 100 training points in the domain, the vector of points in which Equation (10) is evaluated looks like [0.0099; 0.0198; ...; 0.99] m. The solution at $x = 0$ and $x = 1$ m is imposed by the BCs. This vector represents the input of the neural network. In case of very large domains, one could increase the density of points in the regions where the variables are supposed to exhibit a big gradient (i.e. in the penetration depth in the present case). At the same time, locations where the network is evaluated must be scattered in the entire domain.

All calculations of this work made use of the library TensorFlow [38]. NNs are trained on a 16 GB Nvidia Tesla P100 (COLAB). FEM calculations are performed on a i7-7700K Intel CPU equipped with 64 GB of RAM. The training algorithm used to minimize the loss function (Equation (10)) is Adam [37], while all training points are used on a single batch. In this linear case of Maxwell's equations, parameters are chosen as follow: $\mu = \mu_0 = 4\pi 10^{-7}$ H/m, $\sigma = 10^7$ S/m, $\omega = 2\pi$ rad/s.

2.1.1 | Adimensionalization

Choosing a frequency of 1 Hz imposes to have a pretty large domain, here of 1 m, since at the furthest boundary $|\underline{B}|$ is supposed to be zero (Equation (8)). However, this is the result of an adimensionalization and does not represent a restriction. Let us suppose the frequency is 10^5 Hz, and we intend to

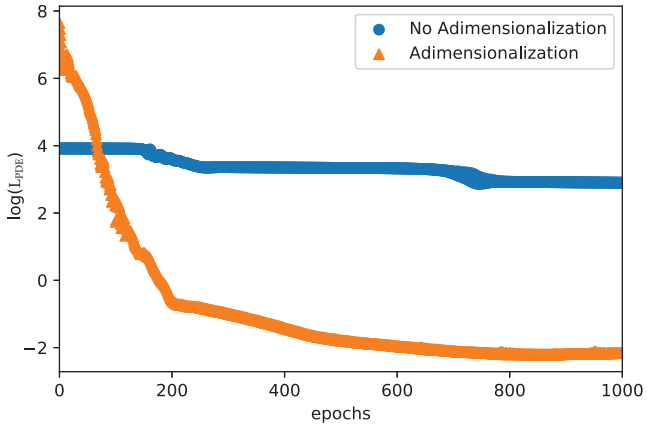

FIGURE 1 Adimensionalization speeds the rate of convergence up

consider the calculation domain (0; 0.01) m. The space could be adimensionalised as follow:

$$\hat{x} = \frac{x}{x_0} \tag{11}$$

Equation (7) becomes:

$$\frac{1}{\mu\sigma x_0^2}\frac{\partial^2 \underline{B}}{\partial \hat{x}^2} = j\omega \underline{B} \tag{12}$$

Assuming in this case $x_0 = 10^{-2}$, one obtains:

$$\frac{1}{\mu\sigma}\frac{\partial^2 \underline{B}}{\partial \hat{x}^2} = j\hat{\omega} \underline{B} \tag{13}$$

where $\hat{\omega} = 20\pi$ rad/s and $\hat{x} \in (0;1)$ m. Moreover, as visible in Figure 1, space adimensionalization speeds significantly the rate of convergence up.

Since an analytical solution of Equation (7) exists [36], different architectures of the NN have been tested aiming to study the trade-off between accuracy of the solution and training time. We introduced a "performance factor", PF $= \mathcal{E}$ log(TT), where $\mathcal{E}$ is the error (Equation (14)) between the NN's and analytical solution. The calculation of the error is based on the 100 training points within the domain. Using 100 training points is the outcome of a trial and error approach that has revealed how more points would not justify the increase of training time (TT) in terms of accuracy. On the contrary, going below 100 training points is detrimental for the solution's precision.

$$\mathcal{E} = \frac{\int |T_{f,Re} - \Re(B_{ref})|dx}{\int |\Re(B_{ref})|dx} + \frac{\int |T_{f,Im} - \Im(B_{ref})|dx}{\int |\Im(B_{ref})|dx} \tag{14}$$

Six different configurations (Arch1, ..., Arch6) are compared. They differ in terms of number of neurons, hidden layers, connection between layers, activation function. Max based activation functions are preferred since they do not saturate for positive values and they are quite fast to compute [4, 39].

- Arch1: Two hidden layers with ten neurons each, activation function is $\max(0, x)$;

TABLE 1 Performance factor (PF) with different NN's architectures

	250 epochs	500 epochs	1000 epochs	2000 epochs
Arch1	4.10E+00	5.15E+00	5.89E+00	7.65E+00
Arch2	1.66E+00	5.62E−01	6.63E−01	1.25E−01
Arch3	3.97E−01	1.08E−01	2.02E−02	1.51E−02
Arch4	2.53E−01	4.28E−02	2.72E−02	1.33E−01
Arch5	8.11E−02	1.27E−02	5.07E−03	6.50E−03
Arch6	2.26E−01	4.48E−02	7.83E−03	5.32E−03

- Arch2: Two hidden layers with ten neurons each, activation function is $\max(0, x^3)$ [40];
- Arch3: Two hidden layers with 30 neurons each, activation function is $\max(0, x^3)$;
- Arch4: Two residual blocks [39], each containing 2 hidden layers with 30 neurons, activation function is $\max(0, x^3)$;
- Arch5: Two residual blocks, each containing 2 hidden layers with 60 neurons, activation function is $\max(0, x^3)$;
- Arch6: Two hidden layers with 60 neurons each, activation function is $\max(0, x^3)$;

We will mostly use architectures 5 and 6, motivated by the results visible in Table 1. Figure 2 includes the comparison between the analytical solution and the trial functions after the NN has been trained for 500 epochs (4.5 s training time with architecture 6, loss is 1.96E−02). The network works equally well when the phase of $\underline{B}$ at $x = 0$ is non-zero (see Figure 3).

2.2 | Non-linear Maxwell's equations neglecting magnetic losses

EM devices make a widespread use of ferromagnetic materials [41]. Ferromagnetic materials are a certain group of substances that tend to manifest or display strong magnetism in the direction of the field due to the application of a magnetic field. In general, the relation between the applied magnetic field and magnetic flux density is not a single-valued. Indeed, the material shows memory effects, the so-called "hysteresis". However, in the modelling of electromagnetic devices, it is a common practise to employ a "single-valued B–H curve" [42]. In this work, the Froehlich's equation is used [43]:

$$|\underline{B}| = \frac{|\underline{H}|}{a + b|\underline{H}|} \tag{15}$$

where a, b are two material dependent constants, $|\underline{B}|$ and $|H|$ are the modules of magnetic flux density and magnetic field, respectively. Here it is assumed no phase shift between $\underline{B}$ and $\underline{H}$. It is noteworthy to underline that Equation (15) is not the DC B–H curve, but it is an equivalent one that can be used in time harmonic analysis. In fact, locally, in a time harmonic

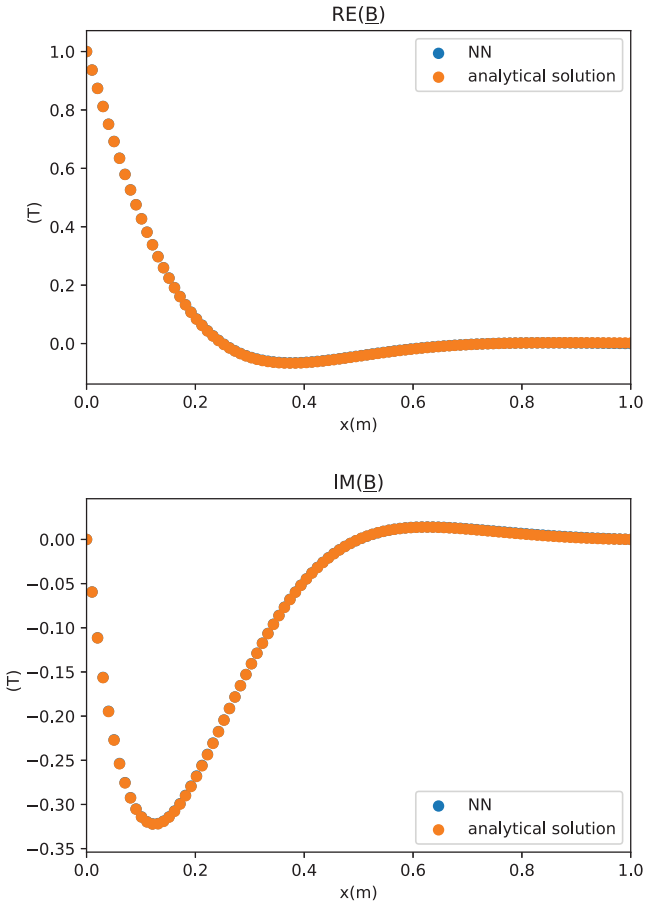

FIGURE 2 Linear Maxwell (real part of $\underline{B}$, $B_{\mathrm{Re}}(0) = 1$, imaginary part of $\underline{B}$, $B_{\mathrm{Im}}(0) = 0$): comparison between the NN's and the analytical solution (curves optically coincide)

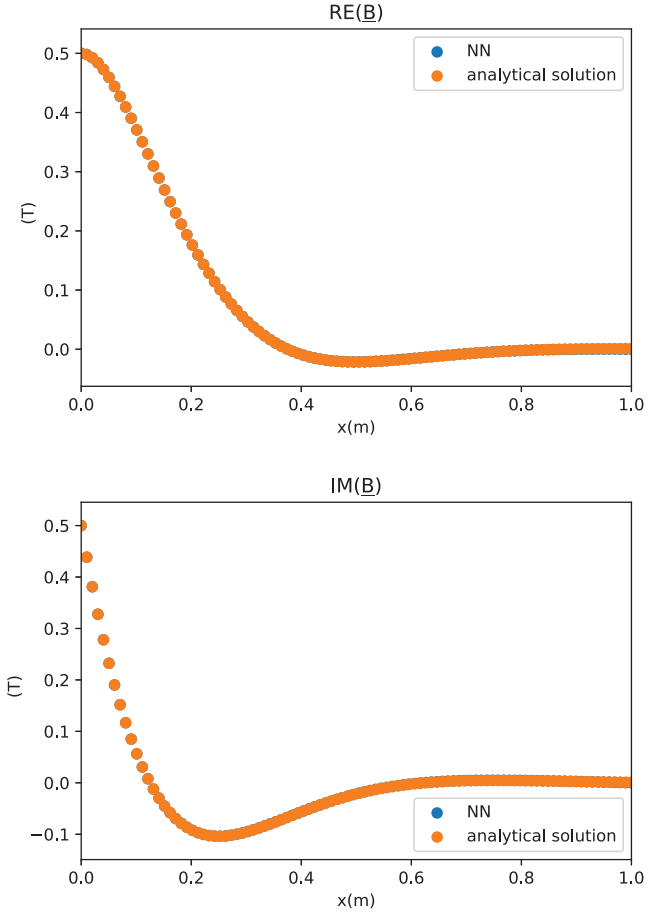

FIGURE 3 Linear Maxwell (real part of $\underline{B}$, $B_{\mathrm{Re}}(0) = 0.5$, imaginary part of $\underline{B}$, $B_{\mathrm{Im}}(0) = 0.5$): comparison between the NN's and the analytical solution (curves practically coincide)

simulation, the value of permeability is constant throughout a period. For this reason, an equivalent B–H relation is needed [44]. The NN in the non-linear case has three outputs ($\mathcal{N}_1(x)$, $\mathcal{N}_2(x)$, $\mathcal{N}_3(x)$), relative to $|\underline{H}|$, $|\underline{B}|$, and ϕ, respectively, each with a different trial function:

$$\begin{aligned} T_{\mathrm{f},H} &= \mathcal{N}_1(x)\, m_H\, x\, (1-x) + H_0(1-x) \\ T_{\mathrm{f},B} &= \mathcal{N}_2(x)\, m_B\, (1-x) \\ T_{\mathrm{f},\phi} &= \mathcal{N}_3(x)\, m_\phi\, x + \phi_0(1-x) \end{aligned} \tag{16}$$

H_0 and ϕ_0 are respectively the magnetic field intensity and the phase at $x = 0$. In this test case, they value 1000 A/m and 0 rad, while a, b, and σ are equal to 5000, 0.45, and 10^5 S/m, respectively. m_H, m_B, m_ϕ are typically chosen one order of magnitude higher than the expected maximum field values (i.e. 10^5, 10^1, 10^0, respectively). Frequency and calculation domain remain unchanged. As before, the trial functions automatically satisfy the Dirichlet BCs. The loss function must also take into account for the B–H relation:

$$\mathcal{L} = \mathcal{L}_{\mathrm{PDE}} + \frac{10^2}{\mathrm{TP}} \sum_{\mathrm{TP}} \left\| T_{\mathrm{f},B} - \frac{T_{\mathrm{f},H}}{a + bT_{\mathrm{f},H}} \right\|_2 \tag{17}$$

where $\mathcal{L}_{\mathrm{PDE}}$ refers to Equation (5):

$$\begin{aligned} \mathcal{L}_{\mathrm{PDE}} = \frac{1}{\mathrm{TP}} \sum_{\mathrm{TP}} \Bigg(& \left\| \frac{1}{\sigma} \nabla^2 T_{\mathrm{f},H} \cos(T_{f,\phi}) + \omega T_{\mathrm{f},B} \sin(T_{\mathrm{f},\phi}) \right\|_2 \\ & + \left\| \frac{1}{\sigma} \nabla^2 T_{\mathrm{f},H} \sin(T_{\mathrm{f},\phi}) - \omega T_{\mathrm{f},B} \cos(T_{\mathrm{f},\phi}) \right\|_2 \Bigg) \end{aligned} \tag{18}$$

The weight 10^2 is a heuristic choice. Results of the NN are compared to those obtained with the commercial FEM package ANSYS Mechanical Apdl. ANSYS Apdl models non-linear ferromagnetic material in time harmonic analysis replacing the DC B–H curve by another fictitious B–H expression based on average energy equivalence [45, 46]. The calculation time required by the FEM solution is approximately 1.2 s. In ANSYS it is also possible to self-implement other equivalence methods for modelling ferromagnetic materials, for instance when the "effective" magnetization curve is known. In this case, in each element, the value of the magnetic permeability is adapted to the magnetic field strength. Nine iterations are enough to reduce the rate of change after every iteration below 0.1%. However, the calculation time grows to 8.6 s. Two case studies have been analysed:

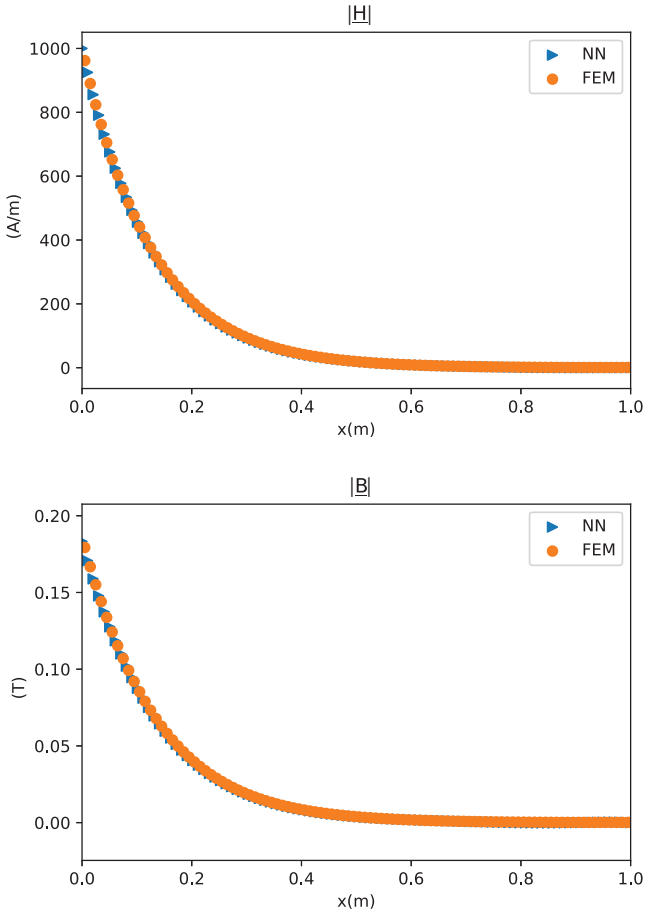

FIGURE 4 Non-linear Maxwell: comparison between the NN's and FEM solution

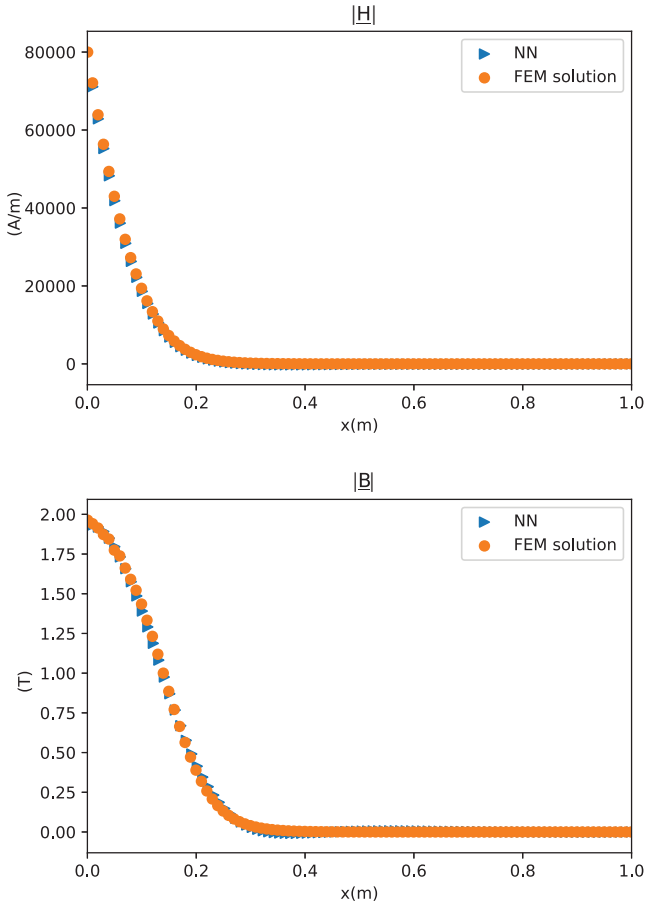

FIGURE 5 (Pronounced) Non-linear Maxwell: comparison between the NN's and FEM solution

the first one with a relative low magnetic field intensity ($H_0 = 1000$ A/m, $\sigma = 10^5$ S/m), the second one with a pronounced non-linearity ($H_0 = 80$ kA/m, $\sigma = 10^6$ S/m). In the first case 750 epochs (6.8 s training time using architecture 6, average loss $1.9E-02$) are enough in order to achieve a satisfactory accuracy (Figure 4, $\mathcal{L} = 1.52E-02$). In the second one, the results after 3000 epochs (19.7 s training time with architecture 6) are visible in Figure 5 ($\mathcal{L} = 4.51$E+00). Average loss is 2.78E+00. Referring to $\underline{B}$, assuming the FEM solution as reference, the global error (Equation (14)) is equal in the first and second case to 2.21E−02 and 2.97E−02, respectively.

So far, we have assumed that in the case of the NNs, nets are initialised at every training. Similarly, in FEM models, the geometry and the mesh have been built at every simulation. In engineering we are often asked to solve inverse problems, for instance, in order to design a device or to determine unknown parameters, like material properties. This means that PDEs must be solved hundreds or thousands of times. If it is the case, avoiding, at every simulation, to initialize the model could save significant calculation time. If, on the one hand, this is hardly feasible with a FEM commercial software, on the other, its applicability to NNs is straightforward. With reference to the first case, if we take an already trained NN and we use it as a starting point with a new B–H curve, 300 epochs are enough to reach a loss of 1.07E−02 with a training time of 1.6 s. Similarly in the second example, 1000 epochs could allow to achieve a loss of 1.81E+00 in 5.6 s. In conclusion, whenever the material properties or boundary conditions change, the neural network must be trained because the solution of the PDE has changed. However, using a pre-trained network could lead to a meaningful reduction in training time.

Equation (17), as aforementioned, does not refer to the DC B–H curve, but to an equivalent expression for the time harmonic analysis. However, the equation of this curve is not always available. In literature, several methods have been developed aiming at transforming the DC B–H function into an equivalent dependency for time harmonic simulations. Effective magnetization, RMS method, energy, enhanced co-energy are the most well-known approaches [44, 51, 53, 54]. A RMS method consists of assigning, at each $|\underline{H}|$ field value, the magnetic flux density it has supposed to have at $|\underline{H}|/\sqrt{2}$. Its implementation is cheap and straightforward, since Equation (17) turns into:

$$\mathcal{L} = \mathcal{L}_{\text{PDE}} + \frac{10^2}{\text{TP}} \sum_{\text{TP}} \left\| T_{\text{f},B} - \frac{T_{\text{f},H}}{\frac{a}{\sqrt{2}} + bT_{\text{f},H}} \right\|_2 \tag{19}$$

However, in the present work we will refer to the enhanced co-energy approach. The co-energy is defined as the area under the B–H path and has unit of energy. Although this quantity has no physical meaning, it allows to well approximate the losses in time harmonic regime. There are three different definitions of co-energy. The magnetic co-energy:

$$w_{\mathrm{mc}}(|\underline{H}|) = \int_0^{|\underline{H}|} |\underline{B}(h)|\,\mathrm{d}h \tag{20}$$

The flux density amplitude:

$$w_{\mathrm{fd}}(|\underline{H}|) = \frac{1}{2}|\underline{B}(|\underline{H}|)|\,|\underline{H}| \tag{21}$$

The enhanced co-energy:

$$w_{\mathrm{ec}}(|\underline{H}|) = \frac{1}{2}\left[w_{\mathrm{mc}}(|\underline{H}|) + w_{\mathrm{fd}}(|\underline{H}|)\right] \tag{22}$$

As the first two approaches, respectively, overestimate and underestimate the power losses in the time harmonic solution, the enhanced co-energy is generally preferred [51]. The equivalent magnetic flux density is:

$$|\underline{B}_{\mathrm{eq}}| = \frac{2w_{\mathrm{ec}}(|\underline{H}|)}{|\underline{H}|^2}\,|\underline{H}| = \frac{\int_0^{|\underline{H}|} |\underline{B}(h)|\,\mathrm{d}h}{|\underline{H}|} + \frac{|\underline{B}(|\underline{H}|)|}{2} \tag{23}$$

Equation (17) becomes here:

$$\mathcal{L} = \mathcal{L}_{\mathrm{PDE}} + \frac{10^2}{\mathrm{TP}}\sum_{\mathrm{TP}}\left(\left\| T_{f,B} - \frac{\int_0^{T_{f,H}} \frac{h}{a+bh}\,\mathrm{d}h}{T_{f,H}} - \frac{T_{f,H}}{2(a+bT_{f,H})}\right\|_2\right) \tag{24}$$

However, for numerical reasons, it is preferable to remove the magnetic field intensity from the denominator. The loss function is thus:

$$\mathcal{L} = \mathcal{L}_{\mathrm{PDE}} + \frac{10^{-5}}{\mathrm{TP}}\sum_{\mathrm{TP}}\left(\left\| T_{f,H}T_{f,B} - \int_0^{T_{f,H}} \frac{h}{a+bh}\,\mathrm{d}h - \frac{T_{f,H}^2}{2(a+bT_{f,H})}\right\|_2\right) \tag{25}$$

The weight 10^{-5} is the results of a heuristic choice. Architecture 6 was employed. In order to reach a satisfactory accuracy, the first case study (H_0 = 1000 A/m) required 1000 epochs ($\mathcal{L} = 2.4E-02$, elapsed time is 26.8 s). The second case (H_0 = 80 kA/m) needed 5000 epochs instead ($\mathcal{L} = 7.6E+00$, elapsed time is 112.4 s). Pre-training the network can significantly shorten the training time (9.6 s in the first case with 300 epochs and $\mathcal{L} = 1.2E-02$; 22.8 s in the second case with 1000 epochs and $\mathcal{L} = 9.6E+00$). This approach will be further used in Section 4.

2.3 | Non-linear Maxwell's equations including magnetic losses

In the previous section, the magnetic permeability has been supposed to be a real number. That implies the losses in the material come only from the eddy currents. However, ferromagnetic materials show hysteretic effects that are associated with magnetic losses. Indeed, the area of the hysteresis loops represents the magnetic loss per volume unit. In the framework of a time harmonic analysis, a complex magnetic permeability can model the magnetic losses [47–49]:

$$\dot{\mu} = \mu' + j\mu'' = |\dot{\mu}|e^{j\psi} \tag{26}$$

That implies a phase shift between $\underline{B}$ and $\underline{H}$. The NN has now four outputs, the first two ($\mathcal{N}_1(x)$, $\mathcal{N}_2(x)$) responsible of $|\underline{H}|$ and $|\underline{B}|$, the last two ($\mathcal{N}_3(x)$, $\mathcal{N}_4(x)$) refer to ϕ_H and ϕ_B instead. The trial functions are analogous to those of Equation (16). At $x = 0$ it is imposed the value of $H_0 = 10$ kA/m and $\phi_{H_0} = 0$. The loss function looks like:

$$\mathcal{L} = \mathcal{L}_{\mathrm{PDE}} + \mathcal{L}_{\mathrm{BH}} + \mathcal{L}_{\phi} \tag{27}$$

where $\mathcal{L}_{\mathrm{PDE}}$ and $\mathcal{L}_{\mathrm{BH}}$ are similar to those already presented in the previous section, while the last term is equal to:

$$\mathcal{L}_{\phi} = \frac{10^3}{\mathrm{TP}}\sum_{\mathrm{TP}} \| T_{\mathrm{f},\phi_B} - T_{\mathrm{f},\phi_H} - \psi\|_2 \tag{28}$$

The weight 10^3 is a heuristic choice. It is bigger than the one taken in Equation (17) because the phase shift expressed in radiant is, in absolute values, smaller than the magnetic flux density. A high weight in $\mathcal{L}_{\phi}$ ensures a more balanced relative importance between the different terms of Equation (27). The expression of the losses $\mathcal{P}_{\mathrm{E}}$ due to eddy currents is [49]:

$$\mathcal{P}_{\mathrm{E}} = \int_V \frac{|\underline{J}|^2}{2\sigma}\mathrm{d}V \tag{29}$$

The equation for the magnetic losses is instead:

$$\mathcal{P}_{\mathrm{M}} = \int_V \frac{\omega\mu''|\underline{H}|^2}{2}\mathrm{d}V \tag{30}$$

The value of ψ is assumed constant in the first instance. In Table 2 we show the magnetic losses for different values of ψ. We trained the NN for 10^4 epochs using architecture number 6 (average training time 35.7 s, loss 1.90E+00)

However, the phase of permeability is in many materials magnetic field dependent [49]. Usually, in case of magnetic steels, the stronger is $|\underline{H}|$, the greater is ψ. The approach we are proposing can easily handle this condition by having $\psi(|\underline{H}|)$ in Equation (28). In Figure 6 one can see the results in case of $H_0 = 1$ kA/m, $\phi_{H_0} = 0$, and $\psi = \frac{5}{180\pi} + \frac{5}{180\pi}\arctan(0.001|\underline{H}|)$. This

TABLE 2 Magnetic losses at different values of ψ

ψ (°)	tan ψ	$\mathcal{P}_M$ (W)	$\mathcal{P}_M / \mathcal{P}_{TOT}$ (%)
1	0.0175	46.6	1.4
2	0.0349	105.7	3.2
5	0.0875	264.9	7.4
10	0.1763	553.7	13.8

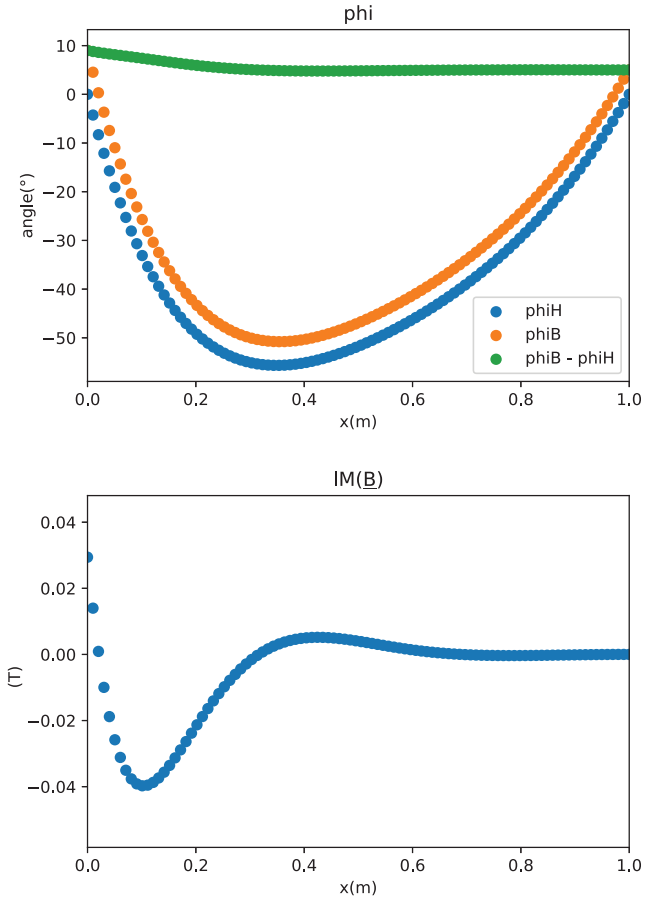

FIGURE 6 Non-linear Maxwell including magnetic losses: the phase change between $\underline{B}$ and $\underline{H}$ increases with growing $|\underline{H}|$

expression of ψ was purely chosen by way of example, in which ψ grows monotonically with $|\underline{H}|$. NN was trained for 10^4 epochs (40.5 s training time, $\mathcal{L} = 1.54\text{E}{+}00$). A direct comparison with ANSYS Apdl is not possible because this software, like many other packages, does not provide the possibility of using a complex permeability. One of the contribution of this work is in fact to show a straightforward approach to estimate how magnetic losses impact total losses. Since only 1D cases are object of analysis in this paper, when dealing with 2D or 3D cases, one can either expand this approach to problems with bigger dimensionality, or increase in a FEM environment the eddy current losses by the magnetic losses got from the NN.

3 | SOLVING MAXWELL'S EQUATIONS IN TIME DOMAIN

3.1 | Linear Maxwell's equations

In this section, we are going to solve Equation (6). This has only an academic interest, since in case of linear materials the equation solved in frequency domain provides the same result (in steady state conditions) at a much lower computational cost. In contrast to the cases presented so far, here also the time appears as a variable. One approach is to consider the time just as the spatial variables. However, we favour here the procedure described in [9], where numerical time stepping is employed. At each time step, the spatial distribution of the magnetic field and flux density is determined. Time derivatives are estimated with a finite difference approach. Since 6 is a diffusion equation, Crank–Nicolson method suits well to this problem. The loss function is in fact:

$$\mathcal{L} = \frac{1}{\mathrm{TP}} \sum_{\mathrm{TP}} \left\| \frac{T_{\mathrm{f},B_{n+1}} - T_{\mathrm{f},B_n}}{\Delta t} - \frac{1}{2\mu\sigma} \left(\nabla^2 T_{\mathrm{f},B_{n+1}} + \nabla^2 T_{\mathrm{f},B_n} \right) \right\|_2 \tag{31}$$

here $T_{\mathrm{f},B_{n+1}}$ is the value of the trial function at the time step $n+1$. The NN has in this case a single output $\mathcal{N}_1$ and, as before, takes the Dirichlet boundary conditions into account:

$$T_{\mathrm{f},B_{n+1}} = \mathcal{N}_1(x)\, m_B \times (1-x) + B_0 (1-x) \sin(\omega \Delta t\, (n+1)) \tag{32}$$

At $t = 0$ the magnetic flux density is supposed to be zero. The number of epochs is not constant for all time steps because the NN requires gradually less epochs to achieve a comparable accuracy. An exponential decay in the number of epochs for each time step is used. Material properties are same like in Section 2.1. The total time is 1 s (frequency is 1 Hz) that has been divided into 100 steps. The architecture number 5 is chosen. Results from the NN (approximately 5000 epochs per each time step, average loss $2.41\text{E}-02$) are in excellent agreement with those obtained with a FD approach (global error taking FD as reference is $4.62\text{E}-03$) (Figure 7). The big number of epochs in comparison to the previous section is motivated by the absolute need to reach a high level of convergence, especially in the first time steps. An imprecise solution would indeed tend to increase the inaccuracy of the results of the following time steps. For this reason, FD outperforms NN in terms of calculation time.

3.2 | Non-linear Maxwell's equations neglecting hysteresis

The Equation (5) has been solved combining the approaches presented so far. A sinusoidal magnetic field H with a peak

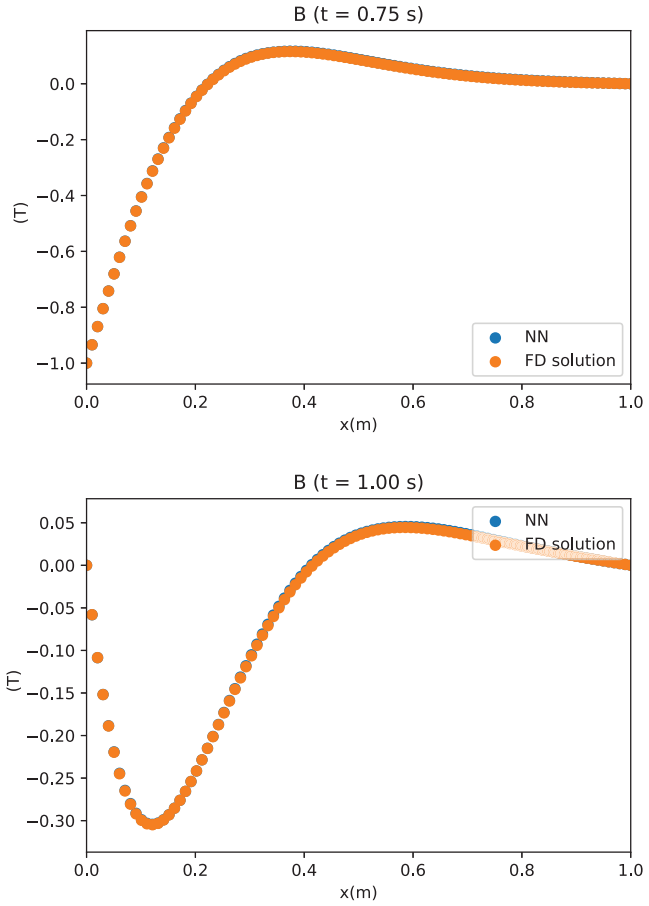

FIGURE 7 Linear Maxwell in time domain (Results at time $t = 0.75$ s and $t = 1.0$ s)

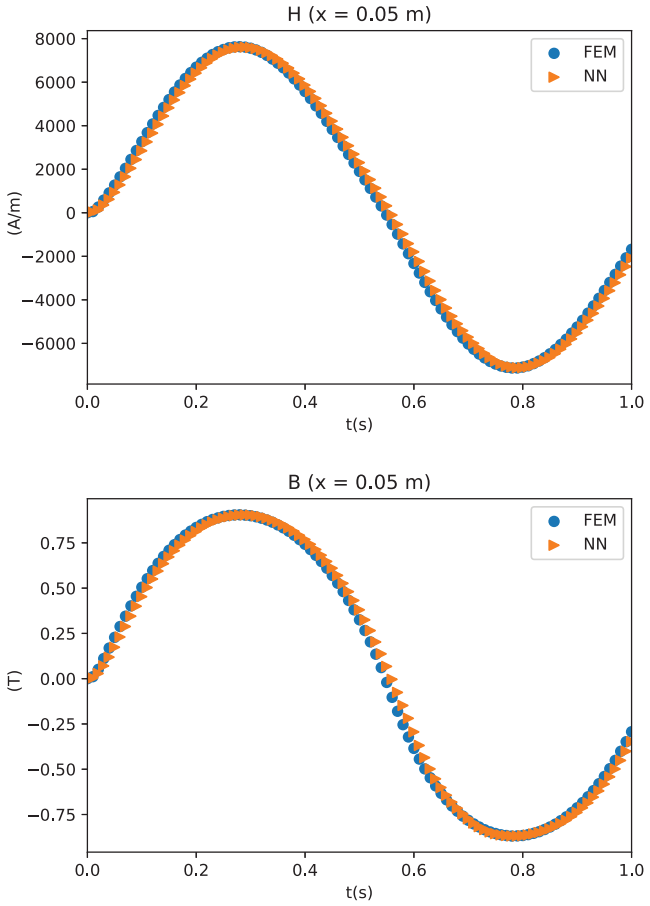

FIGURE 8 Non-linear Maxwell in time domain (H and B at $x = 0.05$ m)

value of 10 kA/m is imposed at $x = 0$ m for $t = [0; 1]$ s. The loss function contains now a second term in order to impose the non-linear law between B and H (similarly to Equation (15)). We show here the time behaviour of H and B at $x = 0.05$ m. The shape of the magnetic flux density is clearly deformed in comparison to the magnetic field because of saturation (Figure 8). The average loss is 2.57E − 02, while each time step has an average of approximately 9000 epochs. In this case the NN requires a longer calculation time in comparison to the FEM model in order to reach similar results (here the global error taking FEM as reference is 3.98E − 02).

3.3 | Non-linear Maxwell's equations including hysteresis

The simulation and design of devices involving magnetic components, such transformers, could require modelling hysteresis effects [52]. Several hysteresis models have been developed in the last hundred years. Among them, the most commonly used and known are the Preisach and Jiles–Atherton (JA) methods [26]. We will stick to the second one, because it is based on the physical behaviour of the magnetic materials. In the original JA [50] model, the magnetization M is decomposed into its reversible M_{rev} and irreversible M_{irr} component ($M = M_{\text{irr}} + M_{\text{rev}}$), corresponding respectively to the reversible and irreversible magnetic domain deformations. The basic equations are:

$$M_{\text{rev}} = c(M_{\text{an}} - M_{\text{irr}}) \tag{33a}$$

$$M_{\text{an}} = M_{\text{s}}\left(\coth\left(\frac{|H_{\text{e}}|}{a} - \frac{a}{|H_{\text{e}}|}\right)\right)\frac{H_{\text{e}}}{|H_{\text{e}}|} \tag{33b}$$

$$\frac{\partial M_{\text{irr}}}{\partial t} = \max\left(0; \frac{M_{\text{rev}}}{ck}\frac{\partial H_{\text{e}}}{\partial t}\right)\frac{M_{\text{rev}}}{|M_{\text{rev}}|} \tag{33c}$$

where $H_{\text{e}} = H + \alpha M$. a, c, α, M_{s}, and k are model parameters for the JA method. A little algebra gives the following two relations:

$$M_{\text{rev}} = \frac{c}{1-c}(M_{\text{an}} - M) \tag{34a}$$

$$\frac{\partial M}{\partial t} = (1-c)\frac{\partial M_{\text{irr}}}{\partial t} + c\frac{\partial M_{\text{an}}}{\partial t} \tag{34b}$$

In this section, two case studies are subject of investigation. In the first example, the system of Equations (33) and (34)

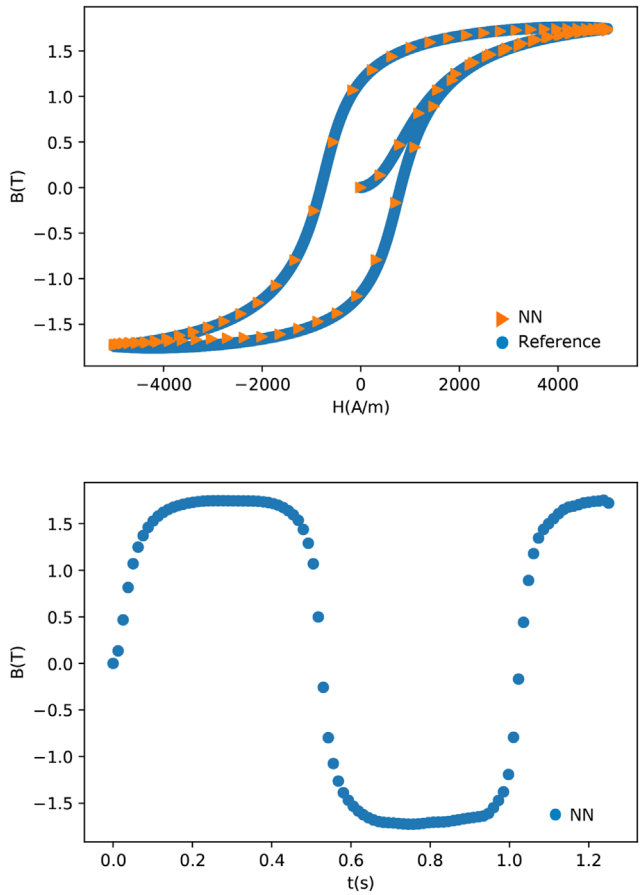

FIGURE 9 Modelling hysteresis with the JA approach (hysteresis loop and Magnetic flux density in time)

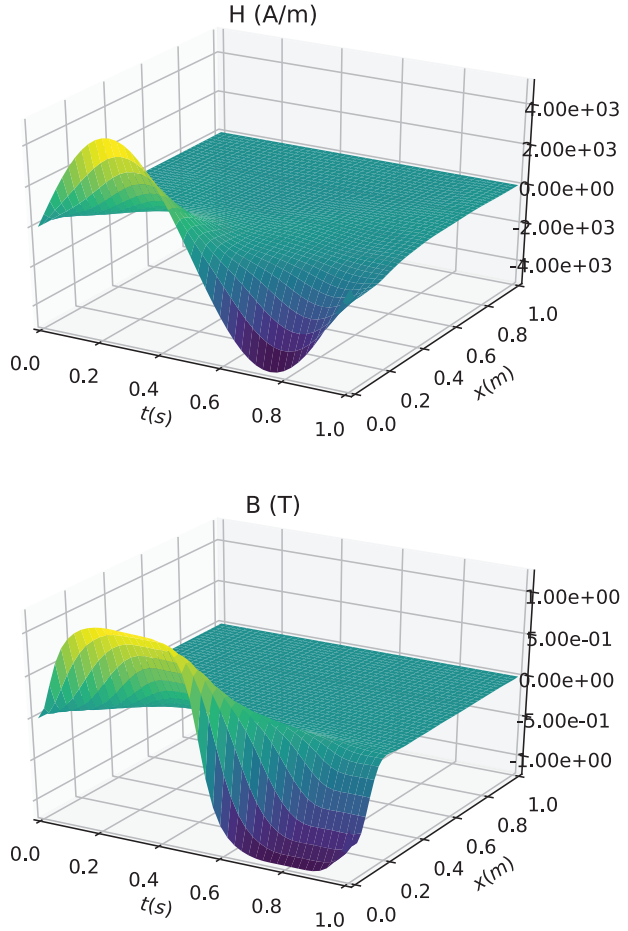

FIGURE 10 Non-linear Maxwell's equations considering hysteresis (H and B field)

is solved using a neural net, aiming at getting the expression of B in time. The excitation field is assumed sinusoidal: $H = 5000\sin(2\pi t)$, where the time is here the only variable in the domain (0; 1.25] s. The NN that provides the solution has only one output, which refers to M. Material parameters are chosen as follow: $a = 700$ A/m, c = 0.1, $\alpha = 0.001$, $M_s = 1.6\,10^6$ A/m, and $k = 1000$ A/m. Properties come from [26]. 100 training points are used, which are uniformly distributed in the domain (0; 1.25] s. The number of epochs is 2.5×10^4, while the loss function refers instead to Equation (34b). A numerical trick is necessary when calculating M_{an}, because the given Equation (33b) has singularities when $|H_e|$ approaches zero. A standard Taylor expansion is used when $|H_e| < 0.1$. Figure 9 summarizes the results. The first picture qualitatively compares the output of the network with the reference (i.e. the solution of equations of JA model obtained numerically). You notice how, at t = 0, $B, H = 0$; with growing H field, the curve of first magnetization takes shape. Once reached the maximum H, B values, with decreasing excitation, B will no longer track the curve of first magnetization.

Finally, as a second case study, we considered a 1D time transient analysis where the JA model is implemented. Equation (5) is solved, now keeping also Equations (33) and (34) into account. A known H sinusoidal field is imposed at $x = 0$ with a peak value of 5 kA/m. The NN has two inputs (time and space) and two outputs (related respectively to H and M). So, unlike what done in the last two sections, the time is now treated as a variable. Therefore, the input is a 100 times 100 matrix, since each input variable has 100 training points. The loss function combines the residual of Equation (5) with the residual of Equation (34b). Training required 1.5×10^5 epochs ($2.5E + 03$ s was the training time). Figure 10 summarizes the results, namely, the time and space behaviour of H and B.

4 | APPLICATIONS

4.1 | Inverse $B - H$ curve identification of carbon steel AISI 4140

Induction heating of metals is a well-known resource efficient technology. In particular, heating carbon steels allows to reach efficiencies up to 90% below the Curie point. A correct material properties knowledge improves the accuracy of numerical simulations [33]. Referring to the AISI 4140 (whose carbon content is approximately 0.42%), the B–H relation (Equation (15)) is described with $a = 270$ and $b = 0.577$ [43]. In case of a magnetic steel, in induction heat treatment applications,

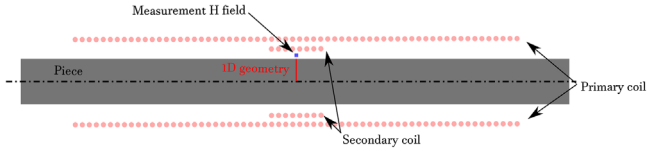

FIGURE 11 Experimental setup for the *B–H* curve identification

TABLE 3 Synthetic data for the inverse *B–H* curve identification (I_1, V_2 are effective values, $|\underline{H}_0|$ refers to the peak value)

I_1 (A)	$\lvert\underline{H}_0\rvert$ (kA/m)	V_2 (V)
20	10.6	7.37
50	33.8	13.33
100	74.4	20.07

magnetic losses play a very minor role [56]. We refer now to the experimental setup of Figure 11. A primary coil with 175 windings (N_1) is supplied with an AC voltage source (frequency is 50 Hz). The secondary (peak up) coil is needed for the measurement of the induced voltage (V_2) and has 20 windings (N_2). The piece is a cylinder with a radius of 50 mm and length of 350 mm. The magnetic field intensity between the secondary coil and the piece could be quantified by a teslameter (the calculation of the magnetic field strength from the magnetic flux density is immediate, known μ_0). No real experiments have been performed with this setup. Synthetic data have been obtained using a 2D axisymmetric time harmonic FEM model (ANSYS based), which reproduced the setup of Figure 11. In addition to the geometry, material properties are required as input parameters for the 2D FEM model. They include the *B–H* curve (a = 270 and b = 0.577) and the electrical resistivity of AISI 4140 (25E−08 Ωm) and copper (2E − 08 Ωm) [43].

Three different excitation currents I_1 have been analysed. Table 3 summarizes the synthetic data obtained with the 2D FEM model. These data are the input parameters for the inverse *B–H* curve identification, which could be formulated as optimization problem:

$$\min_{a,b} \max_{i=1,\dots,3} |V_{2,1D}(|\underline{H}_{0,i}|, a, b) - V_2(|\underline{H}_{0,i}|)| \tag{35}$$

in which $V_{2,1D}$ has been obtained from the model presented in Section 2.2 as:

$$V_{2,1D} = \frac{N_2\omega}{\sqrt{2}}\left(\left[\int T_{f,B}\cos(T_{f,\phi})\,dx\right]^2 + \left[\int T_{f,B}\sin(T_{f,\phi})\,dx\right]^2\right)^{\frac{1}{2}} \tag{36}$$

It means that at each combination of a, b, and $H_0 = |\underline{H}_0|$, the neural network is trained to solve the direct (forward) problem. In the neural network based model, the excitation field is assumed to be H_0 (see Equation (16)), while ϕ_0 is zero. 100 training points have distributed inside the domain (0; 0.05) m. The equivalent *B–H* curve is based on the enhanced co-energy (see Section 2.2 for details relative to the NN's characteristics). Equation (35) is solved coupling the differential evolution (DE) algorithm [55] with the 1D deep learning based field evaluation. With a population of 20 individuals, after 12 generations, the minimum of Equation (35) is supposed to be at a = 320.4 and b = 0.571. In that point, the objective function values 0.539 V. The identified parameters are close to the exact ones. The exact and estimated *B–H* curves show a discrepancy only at very low field intensities (below 2 kA/m) in virtue of the different a value.

4.2 | An electromagnetic–thermal coupled analysis for induction heating

The simulation of an induction heating process always involves at least an electromagnetic solution, in order to determine the distribution of the heat sources, and a thermal solution [24, 31 34]. In order to save computational time, the electromagnetic analysis will be done in harmonic conditions. The thermal field is governed by the Fourier's law, which is a diffusion equation, similarly to Equation (6). A new neural network, which has one input (the space x) and one output ($\mathcal{N}_1$, relative to the temperature) variable, is employed in order to calculate the temperature evolution in time and space. As done in Equation (31), a numerical stepping is employed for handling the time derivative. Here the explicit Euler method is adopted:

$$\frac{T_{n+1} - T_n}{\Delta t} = \frac{\lambda}{d\,c_p}\frac{\partial^2 T_n}{\partial x^2}\frac{1}{x_0^2} + \frac{q}{d\,c_p} \tag{37}$$

subjected to:

$$-\frac{1}{x_0}\frac{\partial T_b}{\partial x} = \frac{h}{\lambda}(T_b - T_\infty) \tag{38}$$

in which λ, d, and c_p indicate thermal conductivity, density, and specific heat, respectively. q represents the heat sources, obtained from the sum of the eddy currents and magnetic losses. Equation (38) is a Robin boundary condition (T_b speaks for temperature at the boundary, i.e. x = 0 m), which takes the thermal losses into account (h is the convective heat transfer coefficient, T_∞ is the temperature of the environment. x_0 is intended to adimesionalize the calculation domain). No Dirichlet BCs must be fulfilled and therefore the trial function will look like:

$$T_{f,T}(x) = m_T\,\mathcal{N}_1(x) \tag{39}$$

m_T is equal to 10^3, since the temperature is not expected to overcome 1000 °C. The BC (Equation (38)) is implemented as a penalty within the loss function. Therefore the loss function contains two members: the first refers to Equation (37), the second to Equation (38). The architecture of the net is the number 5. 100 training points have been used. The number of epochs, which gradually decreases in the successive time steps, is on average, 3×10^4.

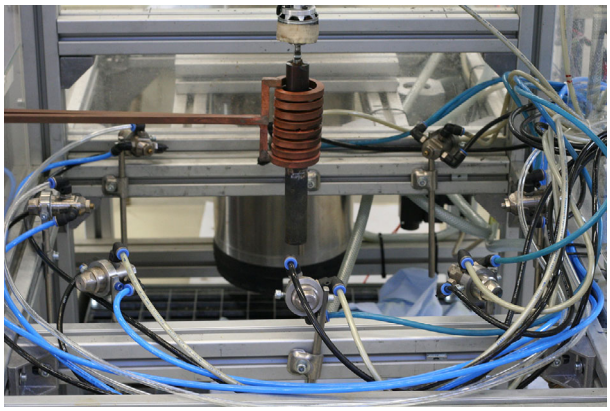

FIGURE 12 Induction heating setup

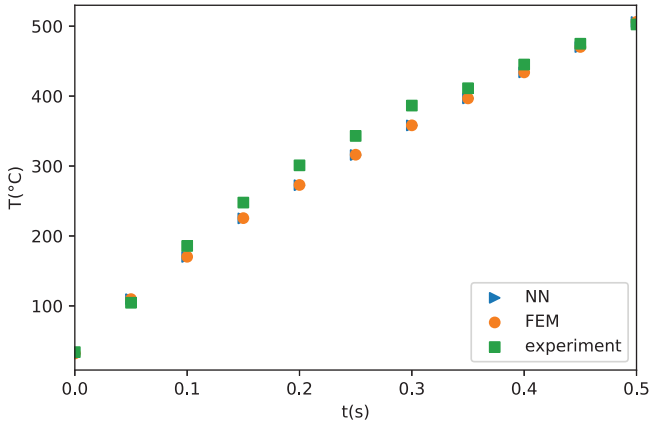

FIGURE 13 Comparison between experiment, NN, and FEM

Real experiments have been carried out to validate the electromagnetic thermal simulations that rely on the neural networks technique (Figure 12). A eight winding inductor is wound around a AISI 4140 billet with 12 mm radius. The inductor's current was monitored with a Rogowski coil, while the surface temperature of the billet, in the central part of the inductor, has been measured by a thermocouple. From the current value and the inductor topology, an estimation of H_0 (excitation field), needed for Equation (16), is obtained. The used material properties are: electrical resistivity 35E−08 Ωm (at 200 °C), *B–H* curve with $a = 270$ and $b = 0.577$, thermal conductivity 41 W/m K (at 200 °C), specific heat 500 J/kg°C (at 200 °C), density 7800 kg/m^3 [43]. The initial and environment temperature is 30 °C, while h is assumed to value 5 W/m^2°C. Finally, the frequency is 12 kHz. The process has a duration of half a second that has been divided into 10 time steps in the simulation. Figure 13 compares the experimental results with the 1D FEM and NN simulations. A good agreement is achieved. Moreover, the absolute difference between FEM and neural networks approach is never higher than 0.6 °C. That confirms the possibility of using a neural networks based method also in induction heating simulations.

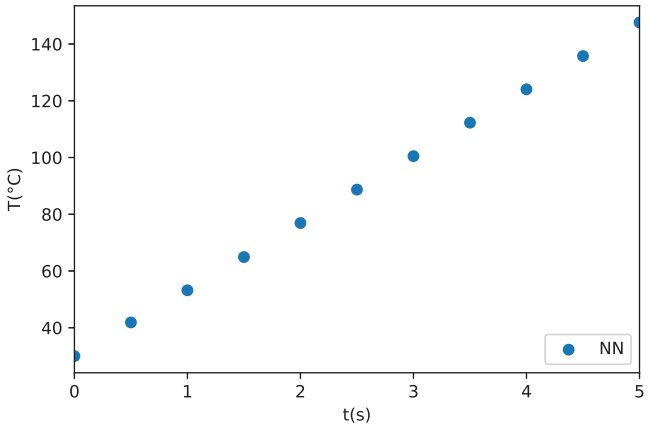

FIGURE 14 Simulated temperature on the surface of the MFC

4.3 | Field analysis for inverse magnetic properties identification of MFCs

The method described in Section 4.2 is here extended to the class of materials that have non-negligible hysteretic behaviours. These include, among others, magnetic flux concentrators (MFCs) for induction applications. In fact, due to the high electrical resistivity, magnetic losses are dominant. In this section, the neural networks based technique uses the approach described in 2.3 for the electromagnetic solution. The thermal analysis is same as in Section 4.2. The aim is to show that our method can potentially be adopted to inverse determine the complex expression of magnetic permeability (Equation (26)). We refer to a case where the flux guiding material is located inside a long cylindrical coil, similarly to the previous examples, such that the field distribution could be assumed locally uniform. It is performed a 1D field analysis (electromagnetic and thermal) in order to find the distribution of temperature in the MFC. Material properties are supposed to be same as for the Fluxtrol 50 [57]: electrical resistivity is 5 Ωm, parameters of the *B–H* curve are assumed to be $a = 12000$ and $b = 0.65$, λ is 6 W/m°C, c_p is 400 J/kg°C, d is 6100 kg/m^3. The only guessed property is ψ (5°). The excitation field H_0 is here supposed 5 kA/m, while the frequency is 100 kHz. In this conditions, the magnetic losses are dominant compared to the Joule losses. Figure 14 depicts the surface temperature in case of a process 5 s long.

5 | CONCLUSIONS

In this paper, MQS Maxwell's equations have been solved in both frequency and time domain making use of artificial neural networks. The flexibility of neural networks can good tackle the non-linearity that characterizes ferromagnetic materials. The proposed approach is to be understood as a straightforward method that fill the gaps of FEM electromagnetic software. In fact, in the linear case, as well as in the non-linear time transient, and harmonic solution with real valued permeability, the FEM solution is usually faster than the NN. However, whenever

a FEM package cannot model, in time or frequency domain, hysteresis, employing the deep learning based approach gives an uncomplicated way of performing a simulation. For instance, it is possible to quantify the hysteretic losses within a flux concentrating material. It was also highlighted how, in general, pretraining NNs further helps to reduce the training time. In this case, the elapsed time could become comparable to that of the FEM model (as in the non-linear time harmonic problem). Despite in this work Maxwell's equations have been solved in 1D domain, some applications do exist. Examples from the inverse magnetic properties identification, as well from induction heating, have been reported. We are currently working on the extension of this approach to the 2D case. The increase of training points seems to be well managed by the deep learning techniques.

ACKNOWLEDGEMENTS

Authors would like to thank the Leibniz Universität Hannover for the support in bearing the publication costs.

AVAILABILITY OF DATA

Research data are not shared.

CONFLICT OF INTEREST

Authors declare no conflict of interest.

ORCID

Marco Baldan https://orcid.org/0000-0002-5803-3150

REFERENCES

1. Chiaramonte, M., Kiener, M.: Solving differential equations using neural networks. Standford Project (2013)
2. Lee, H., Kang, I.S.: Neural algorithm for solving differential equations. J. Comput. Phys. 91(1), 110–131 (1990)
3. Lagaris, I.E., Likas, A., Fotiadis, D.I.: Artificial neural networks for solving ordinary and partial differential equations. IEEE Trans. Neural Netw. 9(5), 987–1000 (1998)
4. Goodfellow, I., Bengio, Y., Courville, A.: Deep Learning, MIT Press, Cambridge, MA (2016)
5. Sirignano, J., Spiliopoulos, K.: DGM: A deep learning algorithm for solving partial differential equations. J. Comput. Phys. 375, 1339–1364 (2018)
6. Berg, J., Nyström, K.: A unified deep artificial neural network approach to partial differential equations in complex geometries. Neurocomputing 317, 28–41 (2018)
7. Wang, Z., Zhang, Z.: A mesh-free method for interface problems using deep learning approach. J. Comput. Phys. 400, 1–16 (2020)
8. Özbay, A.G., et al.: Poisson CNN: Convolutional Neural Networks for the Solution of the Poisson Equation with Varying Meshes and Dirichlet Boundary Conditions, arXiv:1910.08613v1 (2020)
9. Raissi, M., Perdikaris, P., Karniadakis, G.E.: Physics-informed neural networks: A deep learning framework for solving forward and inverse problems involving nonlinear partial differential equations. J. Comput. Phys. 378, 686–707 (2019)
10. Lu, L., et al.: DeepXDE: A deep learning library for solving differential equations, arXiv:1907.04502 (2020)
11. Pang, G., Lu, Lu., Karniadakis, G.E.: fPINNs: Fractional physics-informed neural networks. SIAM J. Sci. Comput. 41(4), A2603–A2626 (2019)
12. Dwivedi, V., Srinivasan, B.: Physics Informed Extreme Learning Machine (PIELM) - A rapid method for the numerical solution of partial differential equations, Neurocomputing 391, 96–118 (2020)
13. Dwivedi, V., Parashar, N., Srinivasan, B.: Distributed physics informed neural network for data-efficient solution to partial differential equations (2020)
14. Meng, X., Karniadakis, G.E.: A composite neural network that learns from multi-fidelity data: Application to function approximation and inverse PDE problems. J. Comput. Phys. 401, 1–15 (2020)
15. Tompson, J., et al.: Accelerating Eulerian fluid simulation with convolutional networks. In: Proceedings of the 34th International Conference on Machine Learning, PMLR 7, Sydney (2017)
16. Xiao, X., et al.: A novel CNN-based Poisson solver for fluid simulation. IEEE Trans. Visual Comput. Graphics 26(3), 1454–1465 (2020)
17. Kissas, G., et al.: Machine learning in cardiovascular flows modeling: Predicting arterial blood pressure from non-invasive 4D flow MRI data using physics informed neural networks. Comput. Methods Appl. Mech. Eng. 358, 1–27 (2020)
18. Pawar, S., et al.: A deep learning enabler for nonintrusive reduced order modeling of fluid flows. Phys. Fluids 31, 085101 (2019)
19. Rumuhalli, P., Udpa, L., Udpa, S.: Finite element neural networks for electromagnetic inverse problems, Rev. Quant. Nondestr. Eval. 21, 728–735 (2002)
20. Tang, W., et al.: Study on Poisson's equation solver based on deep learning technique. In: 2017 IEEE Electrical Design of Advanced Packaging and Systems Symposium, Haining, China (2018)
21. Bartlett, B.: A "generative" model for computing electromagnetic field solutions, Stanford CS229 Projects, 233 Stanford, CA (2018)
22. Zhang, Z., et al.: Solving Poisson's equation using deep learnig in particle simulation of PN junction. In: Proc. of Journal of theInt. Symp. on Electromag. Compatibility, Sapporo, pp. 305–308 (2019)
23. Goldstein, R.: Magnetic flux controller in induction heating and melting, ASM Handbook, Vol. 4C, Induction and Heat Treatment, pp. 633–645 (2014)
24. Baldan, M., et al.: Optimal Design of Magnetic Flux Concentrators in Induction Heating. In: Proceedings of 2019 XXI CSCMP, Samara, pp. 203–207 (2019)
25. Steinberg, T., et al.: Numerical investigation of generative manufactured magnetic flux concentrators for induction heating applications, Proceedings of the XVIII International UIE-Congress, Hannover, pp. 391–396 (2017)
26. Bastos, J.P.A., Sadowski, N.: Electromagnetic Modeling by Finite Element Methods. Marcel Deeker Inc., New York (2003)
27. Turewicz, P.: Multiphysicalische Prozessanalyse zur Erweiterung der Einsatzgrenzen des Kaltwand-Induktions-Tiegelofens, PZH Verlag, Hannover (2013)
28. Brandt, S., Dahmen, H.D.: Elektrodynamik, Springer (2005)
29. Rapetti, F.: Electromagnetic quasi-static models applied to transmission lines. Computing 95(1), S599–S616 (2013)
30. Özakın, M.B., Aksoy, S.: Application of magneto-quasi-static approximation in the finite difference time domain method. IEEE Trans. Magn. 52(8), 7209809 (2016)
31. Di Barba, P., et al.: Sensitivity-based optimal shape design of induction-heating devices. IET Sci. Meas. Technol. 9(5), 579–586 (2015)
32. Sergeant, P., et al.: Thermal analysis of magnetic shields for induction heating. IET Electr. Power Appl. 3(6), 543–550 (2009)
33. Di Barba, P., et al.: Automated B–H curve identification algorithm combining field simulation with optimisation methods and exploiting parallel computation. IET Sci. Meas. Technol. 6(5), 369–375 (2012)
34. Benato, R., Dughiero, F.: Solution of coupled electromagnetic and thermal problems in gas-insulated transmission lines. IEEE Trans. Magn. 39(3), 1741–1744 (2003)
35. Bianchi, N., Bolognani, S., Comelato, G.: Finite Element Analysis of three-phase induction motors: Comparison of two different approaches. IEEE Trans. Energy Convers. 14(4), 1523–1528 (1999)
36. Henke, H.: Elektromagnetische Felder, Theorie und Anwendung. Springer, Berlin (2004)
37. Kingma, D.P., Ba, J.: Adam: A new method for stochastic optimization, arXiv:1412.6980v9 (2014)

38. Abadi, M., et al.: Tensorflow: A system for large-scale machine learning. In: 12th *USENIX* Symposium on Operating Systems Design and Implementation (*OSDI* 16), pp. 265–283 (2016)
39. Geron, A.: Hands-on machine learning with Scikit-Learn, Keras, and TensorFlow, O'Reilly Media (2019)
40. Weinan, E., Yu, B.: The Deep Ritz method: A deep learning-based numerical algorithm for solving variational problems (2017)
41. Di Barba, P., Wiak, S.: MEMS: Field Models and Optimal Design. Springer, Berlin (2020)
42. Abdallh, A.A.: An inverse problem based methodology with uncertainty analysis for the identification of magnetic material characteristics of electromagnetic devices (2012)
43. Schlesselmann, D.: Methoden zur numerischen Berechnung, Analyse, und Auslegung induktiver Randschichthärteprozesse unter Berücksichtigung von magnetischen Sättigungseffekten, PZH Verlag, Hannover (2016)
44. Paoli, G., Biro, O.: Time harmonic eddy currents in non-linear media. COMPEL - Int. J. Comput. Math. Electr. Electron. Eng. 17(5/6), 567—575 (1998)
45. ANSYS Theory Reference, 11th Edition, SAS IP, Inc.
46. Demerdash, D.A., Gillot, D.H.: A new approach for determination of eddy current and flux penetration in nonlinear ferromagnetic materials. IEEE Trans. Magn. 20(4), 682—685 (1974)
47. Bowler, N.: Frequency-dependence of relative permeability in steel. Rev. Prog. Quant. Nondestr. Eval. 25, 1269—1276 (2006)
48. Markel, V.A.: Can the imaginary part of permeability be negative? Phys. Rev. 78, 1–5 (2008)
49. Ivanenko, Y., Nordebo, S.: Measurements and estimation of the complex valued permeability of magnetic steel, lnu.diva-portal.org (2015)
50. Jiles, D.C., Atherton, D.L.: Theory of ferromagnetic hysteresis. J. Magn. Magn. Mater. 61, 48–60 (1986)
51. Labridis, D., Dokopoulos, P.: Calculation of eddy current losses in nonlinear ferromagnetic materials. IEEE Trans. Magn. 25(3), 2665–2669 (1989)
52. Li, H., et al.: A modified method for Jiles-Atherton hysteresis model and its application in numerical simulation of devices involving magnetic materials. IEEE Trans. Magn. 47(5), 1094–1097 (2011)
53. Canova, A., et al.: Simplified approach for 3-d nonlinear induction heating problems. IEEE Trans. Magn. 45(33), 1855–1858 (2009)
54. McKeekin, K., et al.: Improving the accuracy of the time-harmonic FE simulations in induction heating application towards better ferromagnetic material models. COMPEL - Int. J. Comput. Math. Electr. Electron. Eng. 36(2), 526–534 (2017)
55. Storn, R., Price, K.: Differential evolution - a simple and efficient heuristic for global optimization over continuous spaces. J. Global Optim. 11, 341–359 (1997)
56. Valery, R., Loveless, D., Cook, R.: Handbook of Induction Heating. Marcel Dekker Inc., New York (2003)
57. Accessed 8 November 2020, https://fluxtrol.com/inc/pdf/Fluxtrol-50-Specs.pdf

How to cite this article: Baldan M, Baldan G, Nacke B. Solving 1D non-linear magneto quasi-static Maxwell's equations using neural networks. *IET Sci Meas Technol.* 2021;15:204–217. https://doi.org/10.1049/smt2.12022